Journal of Solid State Electrochemistry
https://doi.org/10.1007/s10008-025-06277-2

ORIGINAL PAPER

Tailoring WO_3 photoelectrodes with defect-rich MoO_{3-x} nanosheets for efficient water splitting reaction

Hugo L. S. Santos · Leticia S. Bezerra[1,2] · Pedro H. C. Camargo[1] · Lucia H. Mascaro[1,2]

Received: 22 January 2025 / Revised: 11 March 2025 / Accepted: 12 March 2025

Abstract

Despite its potential for photochemical and photoelectrochemical applications, tungsten trioxide (WO_3) presents limitations due to its wide bandgap and rapid charge carrier recombination. Here, the photoelectrochemical performance of WO_3 films were enhanced by incorporating defect-rich MoO_{3-x} nanosheets. The WO_3 films were produced using a simple polymer-assisted deposition (PAD) method and subsequently modified with defect-rich MoO_{3-x} nanosheets, prepared via solvothermal synthesis, by drop-casting. Electronic microscopy revealed that WO_3 exhibited an agglomerated nano-globular structure with several fissures where the MoO_{3-x} nanosheets were anchored. In terms of photoelectrochemical performance, the optimal WO_3/MoO_{3-x} film exhibited photocurrent densities of 1.30 ± 0.12 mA cm^{-2} and 3.20 ± 0.2 mA cm^{-2} under solar simulator and LED 427 nm illumination, respectively, doubling the photocurrent density of bare WO_3. This enhanced performance was attributed to the formation of a type II heterojunction, which facilitates more efficient charge carrier separation and due to the catalytic enhancement for the oxygen evolution reaction provided by MoO_{3-x}.

Keywords Tungsten oxide · Defect-rich molybdenum oxide · Photoanode · Photoelectrochemical water splitting

Introduction

Turning sunlight into clean fuels that can be stored and moved is crucial for a greener future. Photoelectrochemical (PEC) water splitting, a process that utilizes sunlight to split water into hydrogen and oxygen, stands as a core technology for this proposal. Semiconductor materials are essential for efficient PEC water splitting, as they capture sunlight and convert them into electrons and holes. In this context, tungsten trioxide (WO_3) appears as a promising material for PEC applications. The longer hole diffusion length (~150 nm) compared to α-Fe_2O_3 (2–4 nm), a better electron mobility (~12 cm^2 V^{-1} s^{-1}) compared to TiO_2 (~0.3 cm^2 V^{-1} s^{-1}), and its valence band energetically located below the energy required for several oxidation reaction, between them the oxygen evolution reaction (OER), enables the application of WO_3 as a photoanode.[1, 2]. In addition, this material presents excellent stability in acidic aqueous solutions [3].

While WO_3 exhibits favorable optoelectronic proprieties, its photoelectrocatalytic efficiency towards OER requires significant enhancement. Due to its low absorption coefficient (104–105 cm^{-1}), relatively thick films are necessary to ensure sufficient light absorption in this material [4]. However, thicker films can facilitate charge carrier recombination and diminish OER performance. Moreover, peroxide formation on the WO_3 surface during OER can accelerate photocorrosion, leading to reduced stability [3]. Also, the large indirect bandgap energy, ranging from 2.4 to 2.8 eV, depending on the synthesis method, limits its theoretical maximum solar energy efficiency for hydrogen production to approximately 6% and its theoretical photocurrent density to only 5 mA cm^{-2} under AM 1.5 G solar illumination [5]. To address these limitations, extensive research has focused on strategies such as morphology engineering, heterojunction formation, and cocatalyst modification.

Films of WO_3 can be synthesized with different morphologies, depending on the synthesis method. In this regard, nanostructured morphologies play an important role in photoelectrocatalytic activity, since this type of structure can improve the diffusion of photogenerated charge carriers,

✉ Lucia H. Mascaro
lmascaro@ufscar.br

[1] Department of Chemistry, University of Helsinki, A.I. Virtasen Aukio 1, PO Box 55, N0014 Helsinki, Finland

[2] Department of Chemistry, Federal University of Sao Carlos, 13565-905 Sao Carlos, Sao Paulo, Brazil

Published online: 26 March 2025

increase the light absorption by the semiconductor, and increase the number of active sites due to the larger surface area [6, 7]. Polymer-assisted deposition (PAD) is a convenient technique for fabricating porous, adherent WO_3 films. In this method, a polymer serves as a stabilizing agent, inhibiting particle growth and promoting film adhesion to the substrate [8]. The WO_3 films produced by PAD often exhibit an irregular, porous morphology consisting of nanospheres, which provides a large surface area [9].

Heterojunction is another effective strategy for improving charge separation efficiency and the photoelectrocatalytic activity of a device. The energy alignment between the conduction band (CB) and valence band (VB) of the semiconductors is the main driving force for electron transfer between the materials, increasing charge flow and reducing recombination. WO_3 is frequently used to build heterojunctions with other semiconductors to enhance performance, such as WO_3/CuO [10], WO_3/$BiVO_4$ [11], WO_3/g-C_3N_4 [12] and more recently, and WO_3/MoO_{3-x} [13] for photocatalysis application. Recent studies demonstrate that heterojunctions incorporating MoO_{3-x} significantly enhance the light absorption and energy conversion efficiency. This enhancement is attributed to the localized surface plasmon resonance (LSPR) exhibited by these particles, which allows them to effectively capture visible light [14–16]. In addition, oxygen vacancies in MoO_{3-x} can trap electrons, preventing them from recombining with holes and enhancing the conductivity. This helps to maintain a higher concentration of charge carriers, which can improve the efficiency of photocatalytic processes [13]. Additionally, MoO_{3-x} has a narrower bandgap, allowing it to absorb a wider range of light and generate more charge carriers.

Herein, we report a novel WO_3/MoO_{3-x} photoanode material presenting a superior performance for PEC water splitting successfully produced by polymer-assisted and drop-casting method. The optimal WO_3/MoO_{3-x} film exhibited photocurrent densities of 1.30 ± 0.12 mA cm^{-2} and 3.20 ± 0.2 mA cm^{-2} under solar simulator and LED 427 nm illumination, respectively, doubling the photocurrent density of bare WO_3. This enhanced performance was attributed to the formation of a type II heterojunction, which facilitates more efficient charge carrier separation and due to the catalytic enhancement for the oxygen evolution reaction provided by MoO_{3-x}.

Experimental

All reagents were of analytical grade and used without any additional purification. Tungsten powder (12 µm, 99.9%) and molybdenum powder (3–7 µm, 99.95%) was purchased from Alfa Aesar, polyethyleneimine (PEI) branched (Mw ~ 25.000 by LS), hydrogen peroxide (30%), and F-doped SnO_2 (FTO) substrates with a resistance of $7 \cdot 10^{-6}$ Ω/m were purchased from Sigma-Aldrich.

Synthesis of MoO_{3-x}

0.192 g (2 mmol) of molybdenum powder was dissolved in 3 mL of H_2O_2 30% solution overnight at room temperature producing a yellow solution. Then, 24 ml of ethanol was added to the Mo solution. The ethanolic solution was put on an autoclave and subjected to heat treatment at 150 °C for 12 h with a heating rate of 3 °C/min. The product formed was centrifuged and washed 4 times with water and dried at 60 °C.

MoO_{3-x}/WO_3 thin films

0.5 g of tungsten powder was dissolved in 6 mL of H_2O_2 18% solution overnight at room temperature. Then, the solution was heated up to 90 °C under reflux for 30 min to decompose the excess peroxide (the color of the solution turns slightly yellow). In another flask, 10 mg of PEI was dissolved in 0.6 mL of water, and then 0.6 mL of the solution of W was added to the PEI solution and homogenized using a vortex mixer producing a yellowish pasty ink. The WO_3 films were produced by the drop-casting method, prior to the deposition the FTO substrates were cleaned with acetone and isopropanol for 10 min in an ultrasonic cleaner following by NH_4OH:H_2O_2 1:1 (v/v) solution at 65 °C for 60 min. The films were produced by the drop of 15 µL of the produced ink on 1.0 cm^2 of the substrate. The films were dried at room temperature for 1 h and subjected to heat treatment at 550 °C for 2 h with a heating rate of 5 °C/min. To produce MoO_{3-x}/WO_3, 10 µL/layer of the MoO_{3-x} dispersion 1 mg/mL in isopropanol was dropped under the WO_3 films and dried at 60 °C for 20 min.

Physical characterizations

Morphological characterizations were performed by means of scanning electron microscopy (SEM) images acquired in high-resolution field emission using a ZEISS SUPRATM 35 FEG-SEM, a Hitachi S-4800, or on a Philips XL-30 with an acceleration voltage of 5 kV. For the WO3 and MoO3-x films, transmission electron microscopy (TEM) measurements taken on a Tecnai F20 electron microscope operating at an accelerating voltage of 200 kV were also performed.

Details of the crystal structure were investigated by X-ray diffraction (XRD) using a Rigaku-DMax2500PC with Cu Kα as radiation source with a wavelength of 1.5406 Å, working at 40 kV and with beam current fixed at 30 mA. X-ray diffractograms were obtained with a scanning rate of 0.2° min^{-1} and a step size of 0.02°.

Elemental analysis was carried out on the benchtop SEM TM4000PLUS II Hitachi equipped with an AZtecOneGO detector of the Silicon Drift type.

The chemical environment and oxidation state of the elements were determined by X-ray photoelectron spectroscopy (XPS) using a Scienta Omicron model ESCA 2SR spectrometer with Al Kα (1486.7 eV) as the excitation source. The positions of the peaks were corrected for possible shifts using the adventitious C 1 s peak at 284.8 eV as a reference. For the deconvolution of the high-resolution spectra of the elements, the Shirley function was used as the baseline function and the GL(30) was used for the shape function, which is a convolution of a Lorentzian function with a Gaussian function being 70% Gaussian and 30% Lorentzian. All XPS spectra were treated in the CasaXPS computer program version 2.3.17PR1.1.120.

The optoelectronic characterizations were performed on a NIR-UV–VIS spectrophotometer (Varian, CARY 5G) equipped with a diffuse reflectance module.

Photoelectrochemical characterization

The electrochemical measurements were carried out in a quartz window cell using an $Ag/AgCl/KCl_{sat.}$ as the reference electrode and a platinum wire as counter-electrode. All measurements were carried out in 0.5 mol L^{-1} H_2SO_4 solution at room temperature. A potentiostat/galvanostat (Autolab PGSTAT302N) was used to acquire the electrochemical data. Light emitting diodes (LEDs) of 427 nm and 740 nm (Kessil PR160L) and a solar simulator AM1.5G (LCS-100, Oriel Instruments) were employed as the light sources.

Electrochemical impedance spectroscopy (EIS) was employed to determine the space charge capacitance (C_{sc}) of WO_3 and MoO_{3-x} materials deposited on FTO. C_{sc}^{-2} vs. applied potential plots were constructed to extract the flat-band potential (E_{fb}) by the Mott-Schottky equation (Eq. 1). All measurements were performed at 1000 Hz applying 10 mV of perturbation amplitude.

$$\frac{1}{C_{sc}^2} = \frac{2}{e\varepsilon_r\varepsilon_0 N_D A^2}\left(E - E_{bp} - \frac{\kappa_B T}{e}\right) \quad (1)$$

The incident photon-to-current efficiency (IPCE) was performed using the monochromator from a Quantum Efficiency/IPCE Measurement Kit (Newport QE-PV-SI) and the measurement was carried out point by point with the wavelength ranging from 350 to 500 nm. All potentials reported in this study were converted to a reversible hydrogen electrode (RHE) using the Eq. 2.

$$E_{RHE} = E_{Ag/AgCl} + E^{\circ}_{Ag/AgCl} + (0{,}059 * pH) \quad (2)$$

where E_{RHE} is the potential measured against the reversible hydrogen electrode (RHE), $E_{Ag/AgCl}$ is the applied potential measured against the Ag/AgCl reference electrode, and $E^{\circ}_{Ag/AgCl}$ is the standard potential of the Ag/AgCl reference electrode.

Results and discussion

The WO_3 films were fabricated using the polymer-assisted deposition (PAD) method. Polyethyleneimine (PEI) worked as a binder and stabilizer for the W species, significantly enhancing film adhesion and surface roughness [9]. The SEM surface image of the WO_3 film at low magnification can be seen in Fig. 1a. The WO_3 film exhibited a highly fractured morphology, with cracks uniformly distributed across its surface. High magnifications SEM image (Fig. 1b) indicated that the WO_3 film was composed of agglomerated nanospheres with an average diameter of 46 ± 13 nm. The nanostructure of WO_3 was also confirmed by TEM as shown in Fig. 1c. The thickness of the WO_3 film was determined from the SEM cross-section as shown in Fig. 1d. Although the exact thickness determination was difficult due to the irregularity of the film, the value of 6.3 µm was determined.

Molybdenum oxide nanostructures (MoO_{3-x}) were prepared using a surfactant-free solvothermal synthesis. Molybdenum metal powder was dissolved in hydrogen peroxide, yielding a yellow solution containing complex molybdenum superoxides [17]. The molybdenum superoxide solution was mixed with ethanol and led to hydrothermal treatment in an autoclave reactor. During this process, ethanol partially reduced Mo(VI) species to Mo(V), leading to the formation of non-stoichiometric molybdenum oxide enriched in oxygen vacancies. Morphological characteristics of MoO_{3-x} were evaluated by SEM images, as shown in Fig. 2a. The MoO_{3-x} particles exhibited a nanosheet morphology with an average thickness of 25 ± 7 nm. These nanosheets were formed through the van der Waals stacking of 2D MoO_{3-x} layers [18]. More details of the morphology of MoO_{3-x} can be visualized in the TEM image of Fig. 2b.

To elucidate the dispersion of MoO_{3-x} nanosheets on the WO_3 film, SEM and TEM imaging was performed on the WO_3/MoO_{3-x} 3L film. As shown in Fig. 2c, the MoO_{3-x} nanosheets were predominantly deposited within the cracks of the WO_3 film. Figure 2d provides a magnified view of the interaction between WO_3 and MoO_{3-x}. The image reveals MoO_{3-x} nanosheets involved by the WO_3 nanospheres, suggesting a strong interfacial contact. The SEM image for the WO_3/MoO_{3-x} 3L film, captured u a backscattered electron (BSE) detector, is presented in Figure S1a. The darker structures, corresponding to the MoO_{3-x} nanosheets, are clearly visible within the cracks of the WO_3 film. The elemental

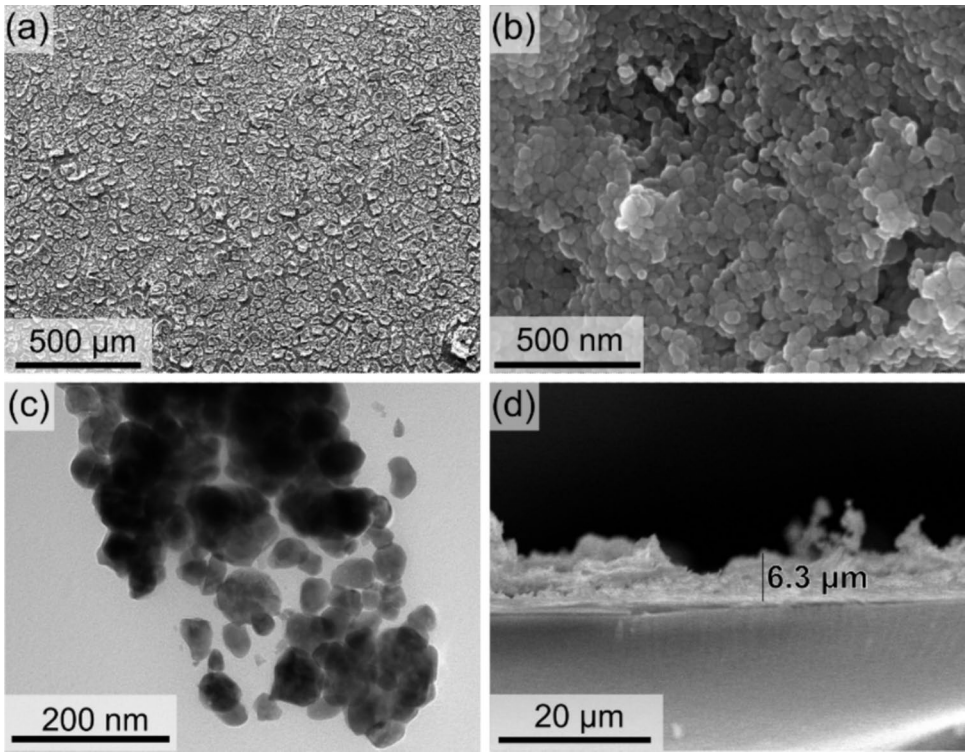

Fig. 1 **a**, **b** SEM surface images of WO_3 films. **c** TEM image for WO_3. **d** SEM image of the cross-section of the WO_3 film

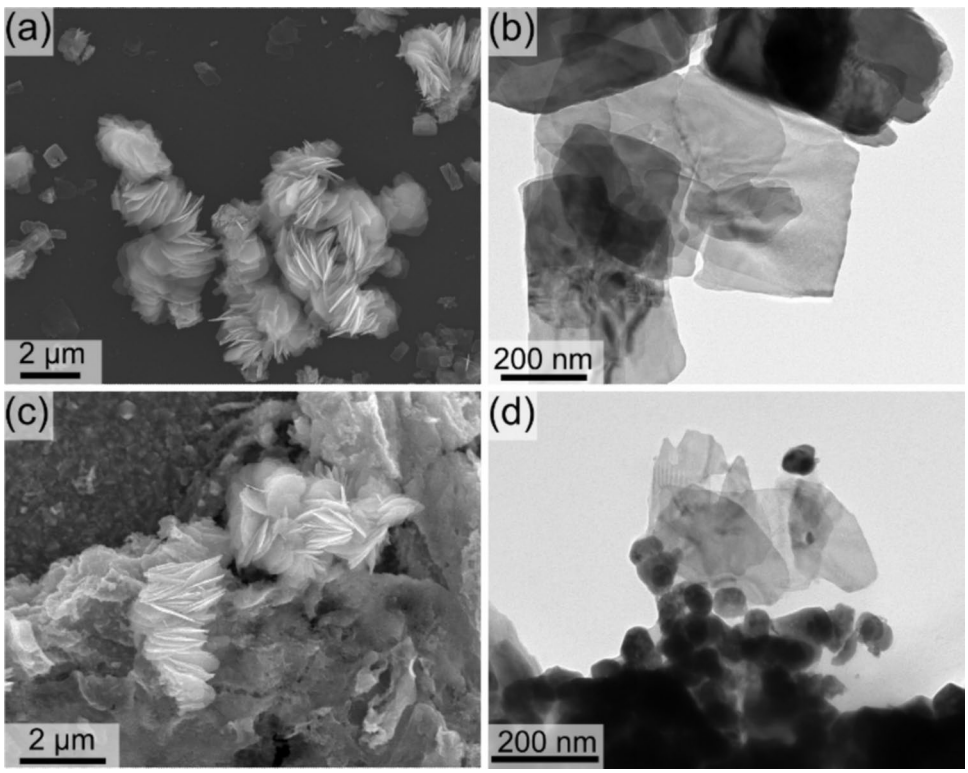

Fig. 2 SEM (**a**) and MET (**b**) images of the MoO_{3-x} nanosheets. SEM (**c**) and MET (**d**) image of the WO_3/MoO_{3-x} 3L film

mapping by EDS for W, Mo, and O, shown in Figures S1b, S1c, and S1d, respectively, provide a clear visualization of the elemental distribution.

The optical properties of WO_3, MoO_{3-x}, and the WO_3/MoO_{3-x} were investigated through UV–vis spectroscopy. Figure 3a presents the absorbance spectra of MoO_3 and

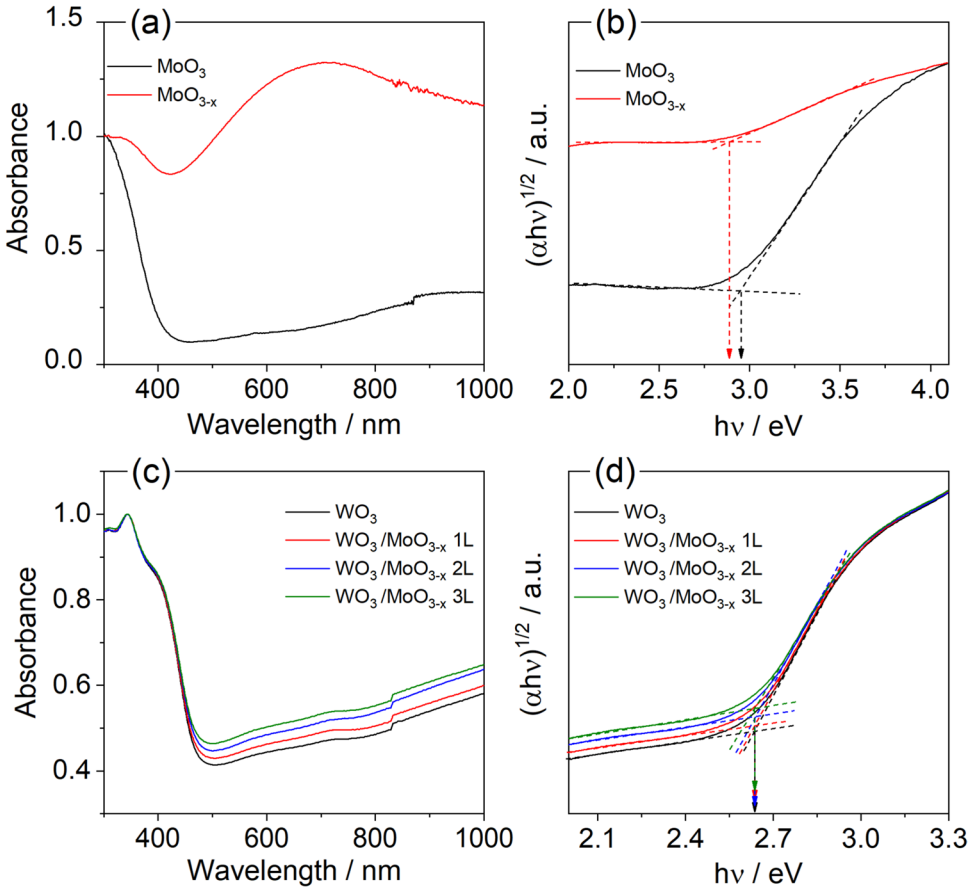

Fig. 3 UV–vis spectra (**a**) and (**c**) for the MoO_3, MoO_{3-x}, WO_3, and WO_3/MoO_{3-x} films. Tauc plots (**b**) and (**d**) for the MoO3, MoO3-x, WO3, and WO3/MoO3-x films

MoO_{3-x}. For reference, MoO_3 was synthesized by annealing MoO_{3-x} at 350 °C for 2 h in air. MoO_3 exhibits a typical semiconductor absorption profile with an onset around 400 nm, corresponding to the usual interband transitions of a semiconductor. In contrast, MoO_{3-x} displays a broad absorption band extending from the near-infrared to the visible region, attributed to localized surface plasmon resonance (LSPR) effects arising from intraband electronic transitions [19, 20]. Additionally, MoO_{3-x} nanosheets show a strong absorption band beginning at 405 nm, which can be assigned to interband excitations, similar to MoO_3. The band gap energy (E_g) of MoO_3 and MoO_{3-x} was determined from Tauc plots using Eq. 3.[21]

$$(\alpha h\upsilon)^n \propto (h\upsilon - E_g) \tag{3}$$

where α represents the absorption coefficient, h is Planck's constant, ν is the frequency of light, and n is an exponent that depends on the type of electronic transition. Given the indirect nature of the transitions in WO_3 and MoO_3, n is assumed to be 1/2 for both materials [18, 22]. Besides that, to distinguish between direct and indirect band gaps, Tauc plots using the n values of ½ and 2 were performed for the bare WO_3 sample as shown in Figure S2. As observed, the Tauc plot using the ½ (indirect, Figure S2a) presented a very clear linear region which can be used to determine the band gap energy. However, the Tauc for $n=2$ (direct, Figure S2b) does not have a clear linear relationship between $(\alpha h\nu)^2$ and $h\nu$, confirming this material has an indirect band gap. Band gap (Eg) values of 2.90 ± 0.03 eV and 2.96 ± 0.05 eV were obtained for two samples. Although a slight numerical variation is observed, the data indicate no statistically significant difference between the samples, as the observed variation is within the combined experimental error.

Figure 3c presents the absorption spectra of bare WO_3 and WO_3/MoO_{3-x} films. No significant alterations in the interband excitation profile were observed for the WO_3/MoO_{3-x} films compared to pristine WO_3. However, a noticeable increase in absorption was detected in the visible to near-infrared region (450–800 nm) with an increasing number of MoO_{3-x} layers. This enhanced visible light absorption in the WO_3/MoO_{3-x} films can be attributed to the localized surface plasmon resonance (LSPR) effect of MoO_{3-x}. The E_g of bare WO_3 and WO_3/MoO_{3-x} was determined from Tauc plots, as illustrated in Fig. 3d. The E_g values remained consistent at 2.65 eV for all samples, indicating that the introduction of MoO_{3-x} layers did not significantly impact the intrinsic band gap of WO_3.

The crystallographic properties of the WO_3 and WO_3/MoO_{3-x} films were investigated using X-ray diffraction (XRD). The resulting diffractograms are presented in Fig. 4a. The diffraction patterns exhibit peaks corresponding only to the monoclinic WO_3 phase (ICSD file no. 50727) and the tetragonal SnO_2 phase originating from the FTO substrate (ICSD no. 16635). The low concentration or amorphous characteristic of MoO_{3-x} in the WO_3/MoO_{3-x} films may account for the absence of detectable MoO_3 peaks in the XRD patterns.

The WO_3 and WO_3/MoO_{3-x} 3C were also characterized by Raman spectroscopy (Fig. 4b). Both films showed four main bands at 272, 330, 713, and 808 cm^{-1}, which are relative to the vibrational modes of the monoclinic phase of WO_3. This corroborates with the XRD diffractograms that exhibited peaks of the monoclinic WO_3 phase. The main vibrational modes observed, pertain to the stretching of the ν(O-W–O) and ν(W–O) bonds at 900–600 cm^{-1} and the bending of the σ(O-W–O) bond in the region of 400–200 cm^{-1} [23, 24]. In addition to the WO_3 vibrational modes, a broad low-intensity band at 994 cm^{-1} was identified only in the spectrum of the WO_3/MoO_{3-x} 3L film and was assigned to the vibrational mode of stretching of the ν(Mo = O) terminal bond, indicating the presence of MoO_{3-x} [25, 26].

The surface chemical composition and oxidation states of the elements in the WO_3/MoO_{3-x} 3L film were determined using X-ray photoelectron spectroscopy (XPS). As shown in the survey spectrum (Fig. 5a), the presence of W, Mo, O, and Sn was confirmed. The inclusion of Sn is attributed to the substrate material. The atomic percentages of W and Mo were calculated to be 85.4% and 14.6%, respectively. The high-resolution XPS spectrum for W 4f (Fig. 5b) exhibits two prominent peaks at approximately 35.8 eV and 38.0 eV, corresponding to W^{6+} $4f_{7/2}$ and W^{6+} $4f_{5/2}$, respectively. These findings align with the XRD analysis, which exclusively revealed peaks associated with monoclinic WO_3 [25, 27]. The high-resolution Mo 4d spectrum (Fig. 5c) was deconvoluted into four distinct peaks at 232.7 eV, 235.9 eV, 231.4 eV, and 234.6 eV, assigned to Mo^{6+} $3d_{5/2}$, Mo^{6+} $3d^{3/2}$, Mo^{5+} $3d_{5/2}$, and Mo^{5+} $3d_{3/2}$, respectively [25, 27]. The atomic percentages of Mo^{6+} and Mo^{5+} were determined to be 88.2% and 11.8%, respectively. It is important to note that the concentration of Mo^{5+} is directly correlated with the concentration of oxygen vacancies (OVs), which is a key factor in the emergence of localized surface plasmon resonance (LSPR) in MoO_{3-x} [28, 29].

Linear sweep voltammetry (LSV) and chronopotentiometry were employed to evaluate the photoelectrocatalytic activity of the films for oxygen evolution reaction (OER). All measurements were conducted in a 0.5 M H_2SO_4 electrolyte solution. Figure 6a presents the LSV curves for WO_3 and WO_3/MoO_{3-x} films under simulated sunlight AM 1.5G (100 mW cm^{-2}). The voltammograms recorded in the dark (dotted lines) exhibited negligible electrochemical activity, indicating the excellent electrochemical stability of the photoanodes within the studied potential range. In terms of photoelectrocatalytic performance, bare WO_3 demonstrated the lowest photoelectrochemical activity with 0.80 ± 0.05 mA cm^{-2}. Conversely, the MoO_{3-x}/WO_3 3L film exhibited the highest response among all samples, achieving a photocurrent density of 1.30 ± 0.12 mA cm^{-2} at 1.23 V_{RHE}, as observed in Table S1. This represents a substantial 60% enhancement compared to bare WO_3. LSVs for all electrodes were also conducted under 427 nm LED illumination (50

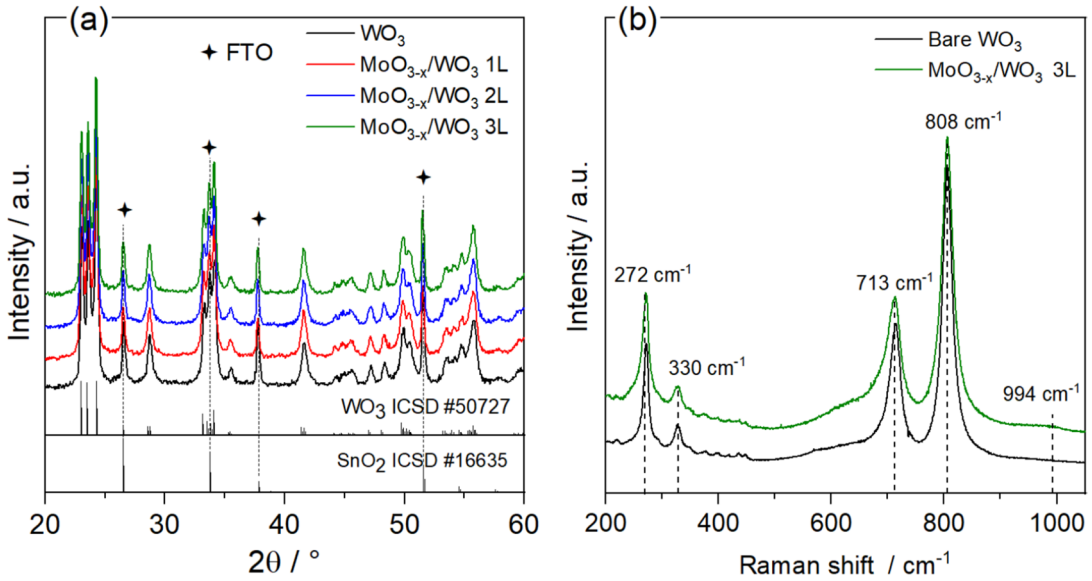

Fig. 4 **A** XRD diffractograms for WO_3 and WO_3/MoO_{3-x} films. **b** Raman spectra for WO_3 and WO_3/MoO_{3-x} 3C films

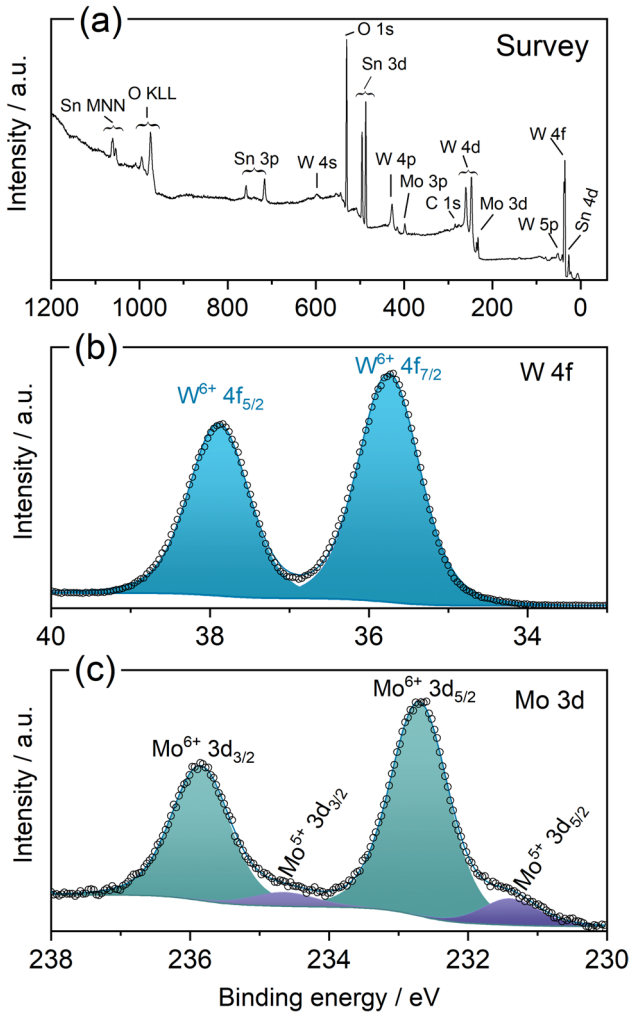

Fig. 5 XPS spectra of survey (**a**), high resolution W 4f (**b**), and high-resolution Mo 3d for WO_3/MoO_{3-x} 3L (**c**)

mW cm^{-2}), as shown in Fig. 6b. The photocurrent generated using the LED was nearly double that observed under simulated solar light. This enhanced photocurrent can be attributed to the superior light absorption properties of WO_3 and MoO_{3-x}/WO_3 under 427 nm LED illumination. The higher energy photons emitted by the LED, which exceed the bandgaps of WO_3 and MoO_{3-x}, result in more efficient excitation of charge carriers. The photoelectrocatalytic activity of all electrodes follows the same trend observed for solar-illuminated experiments, with the MoO_{3-x}/WO_3 3L presenting the highest photocurrent of 3.20 ± 0.2 mA cm^{-2} (Table S1).

LSVs were also recorded under 740 nm LED illumination, as shown in Figure S3. The aim of this experiment was to investigate whether the LSPR effect exhibited by MoO_{3-x} at 740 nm could enhance the photoelectrocatalytic activity of the WO_3/MoO_{3-x} photoelectrodes. It was hypothesized that the "hot" electrons generated in MoO_{3-x} through the LSPR effect could contribute to the OER process. However, no detectable photocurrent was observed for any of the analyzed films. This lack of photocurrent enhancement may be attributed to the inability of the "hot" electrons generated in MoO_{3-x} at 740 nm to be injected into the conduction band of WO_3 due to energetic barriers correlated to the electronic band position.

The incident photon-to-current conversion efficiency (IPCE) is an important parameter to evaluate the conversion efficiency of the incident photon flux to photocurrent, as a function of the wavelength of the light source. The IPCE can be calculated from Eq. 4 [5, 30].

$$IPCE\% = \frac{\left|j\left(mAcm^{-2}\right)\right| \times 1239.8(V \times nm)}{P_{\text{mono}}\left(mWcm^{-2}\right) \times \lambda(nm)} \quad (4)$$

where j is the measured photocurrent density, 1239.8 is the product from the multiplication of Planck's constant (h) by the speed of light (c), P_{mono} is the power of the incident light, and λ is the wavelength of the incident light (nm). The IPCE spectrum, generated using a monochromatic light source, is presented in Fig. 6c. The WO_3/MoO_{3-x} 3L film exhibited significantly higher IPCE values, reaching approximately 79% at 410 nm. The most substantial difference in IPCE between the tested films was observed within the 420–430 nm wavelength range, which corresponds to the LED used in the LSV measurements. While 48% of the photons were converted to photocurrent for WO_3/MoO_{3-x}, only 12.5% were converted by the WO_3 film. This remarkable improvement in performance can be attributed to enhanced interfacial charge transport and more efficient separation of electron–hole pairs [31].

The stability of the pure WO_3 and WO_3/MoO_{3-x} 3L films, a crucial factor in photoelectrocatalysis, was evaluated as shown in Fig. 6d. The photoelectrodes were polarized at 1.1 V_{RHE} for 30 min under 427 nm LED illumination. Both photoanodes exhibited excellent stability during the 30-min test, with negligible current observed in the dark. The initial photocurrent retention was determined using Eq. 5.

$$Retention = \left(\frac{j_f}{j_i}\right) \times 100\% \quad (5)$$

where j_i and j_f represent the initial and final photocurrent densities, respectively. The WO_3/MoO_{3-x} 3L film exhibited the highest initial photocurrent retention, preserving 89.7% of its photocurrent density after 30 min of reaction. In contrast, pure WO_3 retained only 76.5%. This indicates that, in addition to enhancing photoelectrocatalytic activity, the incorporation of MoO_{3-x} also improves the stability of WO_3.

To gain a deeper understanding of the photoelectrochemical performance of WO_3/MoO_{3-x}, the electronic band structures of WO_3 and MoO_{3-x} films were determined. To achieve this, space charge capacitances (C_{sc}) were measured using

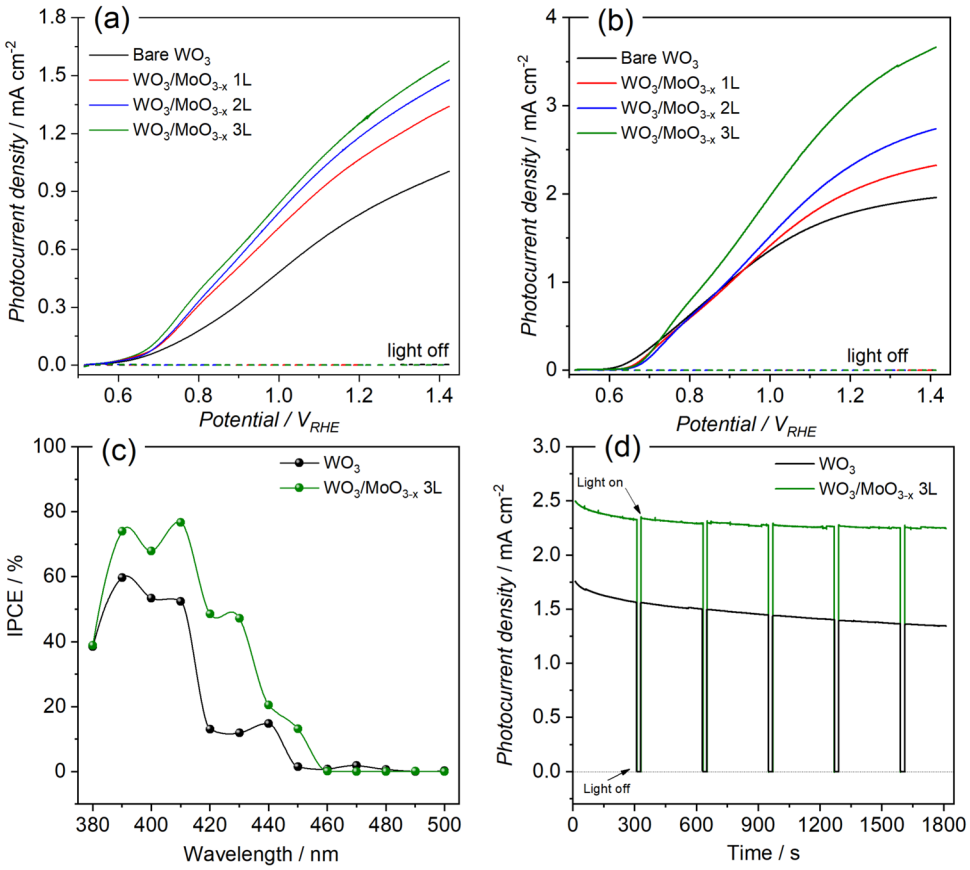

Fig. 6 Linear voltammograms at 10 mV s^{-1} of WO_3 and WO_3/MoO_{3-x} films under illumination of solar simulator (**a**) and LED 427 nm (**b**). IPCE efficiencies (**c**) and stability test (**b**) at 1.2 V_{RHE} for WO_3 and WO_3/MoO_{3-x} 3L films. Experiments performed in 0.5 mol L^{-1} H_2SO_4 solution

electrochemical impedance spectroscopy, and C_{sc}-voltage plots were plotted. The flat-band potential (E_{fb}) can be correlated to C_{sc} using the Mott-Schottky equation (Eq. 1). The C_{sc}-voltage plots for WO_3 and MoO_{3-x} films can be seen in Figs. 7a and b, respectively. The straight-line regions were selected based on the observed linearity in the Mott-Schottky plots. These regions correspond to potential ranges where the depletion region capacitance dominates, as evidenced by the consistent linear relationship between $1/C^2$ and voltage. The selected regions also provided data with minimal noise, ensuring accurate determination of the slope and intercept. Also, to mitigate the discrepancy between the real and geometric surface areas, we fabricated thinner and more compact films of WO_3 and MoO_{3-x} specifically for the M-S analysis. Unlike large nanostructures such as nanowires, the smaller nanospheres of WO_3 and thin sheets of MoO_{3-x} facilitated the creation of compact films with quasi-planar surfaces, minimizing potential errors. The positive slopes in the linear regions confirm the n-type conductivity of these photoelectrodes [18, 32]. The E_{fb}, often considered a good approximation of the conduction band edge (CBE) for n-type semiconductors, was determined to be 0.43 V_{RHE} for WO_3, which is consistent with previously reported values [11]. For MoO_{3-x}, the E_{fb} value was measured as 0.15 V_{RHE}, also aligning with literature reports [33]. The valence band edge (VBE) was determined using the equation $VBE = E_{fb} - E_g$. Table 1 summarizes the values of E_g, E_{fb}, CBE, and VBE for the investigated materials.

An energy band diagram for the WO_3/MoO_{3-x} heterojunction was constructed based on the calculated CBE and VBE values, as depicted in Fig. 7c. The relative positions of these energy levels indicate the formation of a type II n–n heterojunction. This configuration facilitates efficient charge separation due to the staggered alignment of the conduction and valence bands. The resulting potential gradient further enhances the transport of photogenerated charge carriers from the WO_3 to the MoO_{3-x}, where they can participate in redox reactions. Furthermore, MoO_{3-x} may have acted also as a co-catalyst improving the overall photoelectrocatalytic performance of the WO_3/MoO_{3-x} heterojunction. The synergistic combination of these factors, including efficient charge separation, enhanced charge transport, and accelerated reaction kinetics, contributes to the superior photoelectrocatalytic performance of the WO_3/MoO_{3-x} compared to pristine WO_3.

Conclusion

An efficient WO_3/MoO_{3-x} heterojunction was successfully fabricated using straightforward techniques such as polymer-assisted deposition, solvothermal synthesis, and

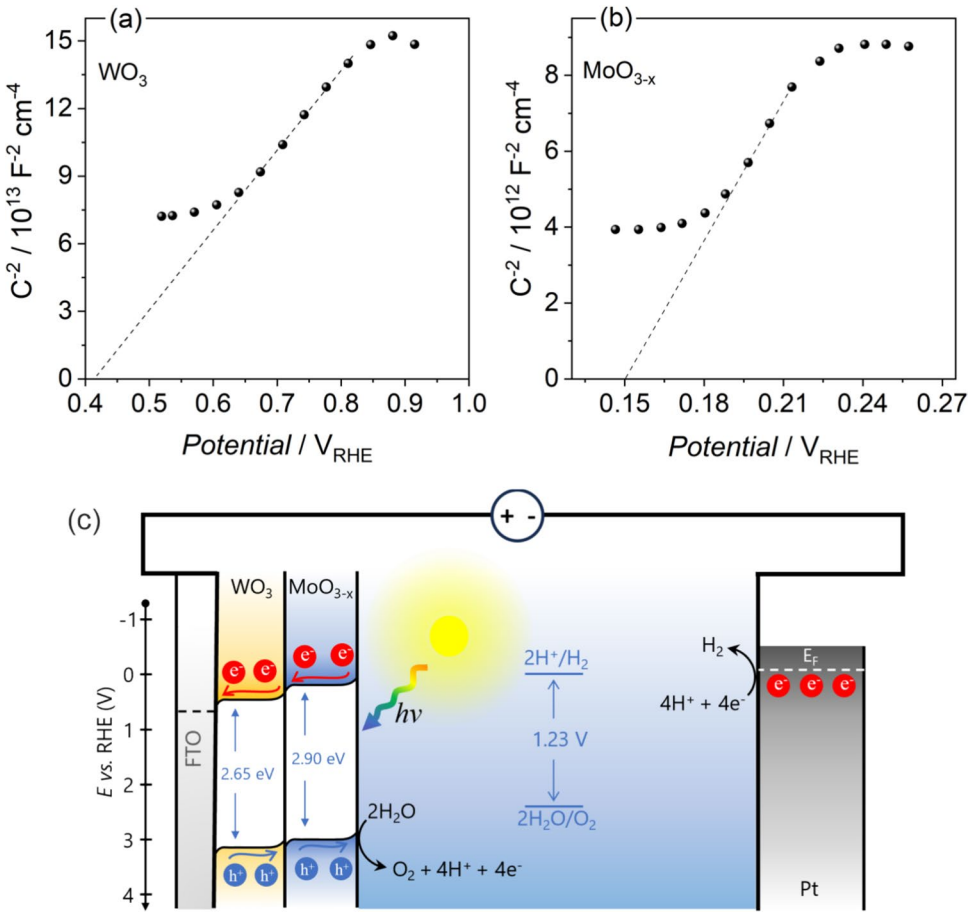

Fig. 7 Mott-Schottky plots at 1000 Hz for WO_3 e (**a**) MoO_{3-x} in 0.5 mol L^{-1} H_2SO_4 (**b**). **c** Illustration of the energy band diagram for the WO_3/MoO_{3-x} heterojunction

Table 1 Optical E_g, E_{fb}, CBE, and VBE values for WO_3 and MoO_{3-x} films

Sample	E_g (eV)	E_{fb} (V_{RHE})	CBE (V_{RHE})	VBE (V_{RHE})
WO_3	2.65	0.43	0.43	3.08
MoO_{3-x}	2.90	0.15	0.15	3.05

drop-casting. By optimizing the number of MoO_{3-x} layers to three, the resulting WO_3/MoO_{3-x} film demonstrated significant enhancement in photoelectrochemical performance, achieving photocurrent densities of 1.30 mA cm^{-2} and 3.18 mA cm^{-2} under simulated sunlight and 427 nm LED illumination, respectively. This substantial improvement, more than doubling the photocurrent density of pristine WO_3, can be attributed to the formation of a type II heterojunction. This configuration facilitates efficient charge carrier separation, preventing recombination losses and promoting charge transport to the surface. Additionally, the incorporation of MoO_{3-x} may have accelerated the kinetics of the rate-determining step, leading to enhanced overall photoelectrochemical performance. These findings highlight the potential of the WO_3/MoO_{3-x} heterojunction as a promising candidate for efficient solar energy conversion and water splitting applications.

Supplementary Information The online version contains supplementary material available at https://doi.org/10.1007/s10008-025-06277-2.

Acknowledgements The authors thank the São Paulo Research Foundation (FAPESP) for the financial assistance to the project and the fellowship granted (#2021/08184-0, #2019/26860-2, #2017/11986-5, and #2013/07296-2); the Conselho Nacional de Desenvolvimento Científico e Tecnológico (CNPq) (#406156/2022-0, #311769/2022-5); FINEP-MCTI 01.22.0179.00 and Shell and the strategic importance of the support given by ANP (Brazil's National Oil, Natural Gas and Biofuels Agency) through the R&D levy regulation.

References

1. Wang S, Liu B, Wang X, Zhang Y, Huang W (2022) Nanoporous MoO3−x/BiVO4 photoanodes promoting charge separation for efficient photoelectrochemical water splitting. Nano Res 15:7026–7033
2. Quang ND, Van PC, Majumder S, Jeong JR, Kim D, Kim C (2022) Optimization of photogenerated charge transport using type-II heterojunction structure of CoP/BiVO4:WO3 for high efficient solar-driver water splitting. J Alloys Compd 899:163292. https://doi.org/10.1016/j.jallcom.2021.163292

3. Zheng G, Wang J, Liu H, Murugadoss V, Zu G, Che H, Lai C, Li H, Ding T, Gao Q, Guo Z (2019) Tungsten oxide nanostructures and nanocomposites for photoelectrochemical water splitting. Nanoscale 11:18968–18994. https://doi.org/10.1039/c9nr03474a
4. Costa MB, de Araújo MA, de Lima Tinoco MV, de Brito JF, Mascaro LH (2022) Current trending and beyond for solar-driven water splitting reaction on WO3 photoanodes. J Energy Chem 1(73):88–113. https://doi.org/10.1016/j.jechem.2022.06.003
5. Chen Z, Dinh HN, Miller E (2013) Photoelectrochemical water splitting: standards, experimental methods, and protocols. Springer, New York
6. Luo J, Steier L, Son MK, Schreier M, Mayer MT, Grätzel M (2016) Cu2O nanowire photocathodes for efficient and durable solar water splitting. Nano Lett 16:1848–1857. https://doi.org/10.1021/acs.nanolett.5b04929
7. Shi W, Zhang X, Li S, Zhang B, Wang M, Shen Y (2015) Carbon coated Cu 2 O nanowires for photo-electrochemical water splitting with enhanced activity. Appl Surf Sci 358:404–411. https://doi.org/10.1016/j.apsusc.2015.08.223
8. Toda-Casaban M, Frontera C, Pomar A, Herrero-Martín J, Alonso JA, Balcells L, Mestres N, Martínez B (2024) Tuning of antiferromagnetic phase in La1–xSrxMnO3 epitaxial thin films by polymer-assisted deposition synthesis. Cryst Growth Des 24:5007–5013. https://doi.org/10.1021/acs.cgd.4c00229
9. Hong SJ, Jun H, Lee JS (2010) Nanocrystalline WO3 film with high photo-electrochemical activity prepared by polymer-assisted direct deposition. Scr Mater 63:757–760. https://doi.org/10.1016/j.scriptamat.2010.05.021
10. Li J, Hu S, Liu S, Hou S, Li L, Huang J (2024) In situ fabrication of WO3/CuWO4/CuO heterojunction photoanode for boosted interfacial charge transfer and enhanced photoelectrochemical water splitting. Int J Hydrogen Energ 3(61):967–74. https://doi.org/10.1016/j.ijhydene.2024.03.004
11. Coelho D, Gaudencio JP, Carminati SA, Ribeiro FW, Nogueira AF, Mascaro LH (2020) Bi electrodeposition on WO3 photoanode to improve the photoactivity of the WO3/BiVO4 heterostructure to water splitting. Chem Eng J 1(399):125836. https://doi.org/10.1016/j.cej.2020.125836
12. Song T, Xie C, Matras-Postolek K, Yang P (2021) 2D layered g-C3N4/WO3/WS2 S-scheme heterojunctions with enhanced photochemical performance. J Phys Chem C 125:19382–19393. https://doi.org/10.1021/acs.jpcc.1c06753
13. Shao Y, You D, Wan Y, Cheng Q, Pan Z (2023) An investigation on a WO3/MoO3−x heterojunction photocatalyst for excellent photocatalytic performance and enhanced molecular oxygen activation ability. React Chem Eng 9:70–81. https://doi.org/10.1039/d3re00396e
14. Katal R, Panah SM, Saeedikhani M, Kosari M, Sheng CC, Leong OS, Xiao G, Jiangyong H (2018) Pd-decorated CuO thin film for photodegradation of acetaminophen and triclosan under visible light irradiation. Adv Mater Interfaces 5:3–10. https://doi.org/10.1002/admi.201801440
15. Zhang X, Chen YL, Liu RS, Tsai DP (2013) Plasmonic photocatalysis. Repo Progres Phys 76(4):046401. https://doi.org/10.1088/0034-4885/76/4/046401
16. Mo J, Barbosa EC, Wu S, Li Y, Sun Y, Xiang W, Li T, Pu S, Robertson A, Wu TS, Soo YL (2021) Atomic-Precision Tailoring of Au–Ag Core-Shell Composite Nanoparticles for Direct Electrochemical-Plasmonic Hydrogen Evolution in Water Splitting. Adv Funct Mater 31(30):2102517. https://doi.org/10.1002/adfm.202102517
17. Li J, Ma L, Huang Y, Jing D (2023) In situ construction of oxygen deficient MoO3-x nanosheets/porous graphitic carbon nitride for enhanced photothermal-photocatalytic hydrogen evolution. Int J Hydrog Energ 48(35):13170–80. https://doi.org/10.1016/j.ijhydene.2022.11.243
18. Wu H, Li X, Cheng Y, Xiao Y, Li R, Wu Q, Lin H, Xu J, Wang G, Lin C, Chen X, Wang Y (2020) Plasmon-driven N2 photofixation in pure water over MoO3-: X nanosheets under visible to NIR excitation. J Mater Chem A Mater 8:2827–2835. https://doi.org/10.1039/c9ta13038a
19. Hoffmann M, Kleine-Weber H, Schroeder S, Krüger N, Herrler T, Erichsen S, Schiergens TS, Herrler G, Wu N-H, Nitsche A, Müller MA, Drosten C, Pöhlmann S (2020) SARS-CoV-2 cell entry depends on ACE2 and TMPRSS2 and is blocked by a clinically proven protease inhibitor. Cell 181:271-280.e8. https://doi.org/10.1016/j.cell.2020.02.052
20. Bezerra LS, Belhout SA, Wang S, Quiroz J, de Oliveira PFM, Shetty S, Rocha G, Santos HLS, Frindy S, Oropeza FE, de la Peña O'Shea VA, Kallio A-J, Huotari S, Huo W, Camargo PHC (2024) Triple play of band gap, interband, and plasmonic excitations for enhanced catalytic activity in Pd/HxMoO3 nanoparticles in the visible region. ACS Appl Mater Interfaces 16:11467–11478. https://doi.org/10.1021/acsami.3c17101
21. Su J, Feng X, Sloppy JD, Guo L, Grimes CA (2011) Vertically aligned WO3 nanowire arrays grown directly on transparent conducting oxide coated glass: synthesis and photoelectrochemical properties. Nano Lett 11:203–208. https://doi.org/10.1021/nl1034573
22. Zhang F, Huang L, Ding P, Wang C, Wang Q, Wang H, Li Y, Xu H, Li H (2019) One-step oxygen vacancy engineering of WO3-x/2D g-C3N4 heterostructure: triple effects for sustaining photoactivity. J Alloys Compd 795:426–435. https://doi.org/10.1016/j.jallcom.2019.04.297
23. Daniel MF, Desbat B, Lassegues JC, Gerand B, Figlarz M (1987) Infrared and Raman study of WO3 tungsten trioxides and WO3, xH2O tungsten trioxide tydrates. J Solid State Chem 67:235–247. https://doi.org/10.1016/0022-4596(87)90359-8
24. Lozano-Rosas R, Lamas DG, Sánchez-Ochoa F, Cocoletzi GH, Karthik TVK, Robles-Águila MJ (2021) CO2 sensing properties of WO3 powder: experimental and theoretical studies. Appl Phys A Mater Sci Process 127:1–14. https://doi.org/10.1007/s00339-021-04960-5
25. Patil MK, Gaikwad SH, Mukherjee SP (2020) Phase- and morphology-controlled synthesis of tunable plasmonic MoO3- x nanomaterials for ultrasensitive surface-enhanced Raman spectroscopy detection. J Phys Chem C 124:21082–21093. https://doi.org/10.1021/acs.jpcc.0c06004
26. Liu Q, Wu Y, Zhang J, Chen K, Huang C, Chen H, Qiu X (2019) Plasmonic MoO3-x nanosheets with tunable oxygen vacancies as efficient visible light responsive photocatalyst. Appl Surf Sci 490:395–402. https://doi.org/10.1016/j.apsusc.2019.06.099
27. Bai H, Yi W, Li J, Xi G, Li Y, Yang H, Liu J (2016) Direct growth of defect-rich MoO3-x ultrathin nanobelts for efficiently catalyzed conversion of isopropyl alcohol to propylene under visible light. J Mater Chem A Mater 4:1566–1571. https://doi.org/10.1039/c5ta08603e
28. Zhang Y, Yu X, Liu H, Lian X, Shang B, Zhan Y, Fan T, Chen Z, Yi X (2021) Controllable synthesis of the defect-enriched MoO3−x nanosheets as an effective visible-light photocatalyst for the degradation of organic dyes. Environ Sci Nano 8:2049–2058. https://doi.org/10.1039/d1en00210d
29. Li Y, Chen X, Zhang M, Zhu Y, Ren W, Mei Z, Gu M, Pan F (2019) Oxygen vacancy-rich MoO 3-: X nanobelts for photocatalytic N 2 reduction to NH 3 in pure water. Catal Sci Technol 9:803–810. https://doi.org/10.1039/c8cy02357c
30. Ji J, Sang P, Kim JH (2021) Improving the photoelectrochemical performance of spin-coated WO3/BiVO4/ZnO photoanodes by maximizing charge transfer using an optimized ZnO decoration layer. Ceram Int 47:26260–26270. https://doi.org/10.1016/j.ceramint.2021.06.035

31. Tang H, Tang Z, Bright J, Liu B, Wang X, Meng G, Wu N (2021) Visible-light localized surface plasmon resonance of WO3- x nanosheets and its photocatalysis driven by plasmonic hot carriers. ACS Sustain Chem Eng 9:1500–1506. https://doi.org/10.1021/acssuschemeng.0c08140
32. Liu Y, Chang YS, Hsu YJ, Hwang BJ, Hsueh CH (2019) Fabrication of WO3 photoanode decorated with Au nanoplates and its enhanced photoelectrochemical properties. Electrochim Acta 321:134674. https://doi.org/10.1016/j.electacta.2019.134674
33. Ren J, Liu Z, Li Q, Chen L, Gong J, Wang H, Li Y, Qu J, Niu R (2024) Harnessing synchronous photothermal and photocatalytic effects of substoichiometric MoO3–x nanoparticle-decorated membranes for clean water generation. ACS Appl Mater Interfaces 16:18855–18866. https://doi.org/10.1021/acsami.4c00516